The structural and electrochemical characterizations of o-$LiMnO_2$ synthesized by one-step hydrothermal process

M. CİHAD KÜÇÜKARSLAN[1,2,*], ÖZLEM DUYAR COŞKUN[1,*]
[1]*Hacettepe University, Department of Physics Engineering, Thin Film Preparation and Characterization Laboratory, Beytepe, Ankara 06800, Turkey*
[2]*Hacettepe University, Institute of Science, Department of Physics Engineering, Beytepe, Ankara 06800, Turkey*

Lithium-ion batteries have been widely researched for academic and industrial applications owing to their high energy density, safety, versatility, and long life in recent years. The cathode material plays a crucial role in determining the energy density, voltage, and overall battery performance. Among cathode materials, o-$LiMnO_2$ has a higher energy density and operating voltage than its counterparts in other phases and structures. Herein, we successfully synthesized o-$LiMnO_2$ without impurities or secondary phase formation by controlling the temperature of hydrothermal synthesis. We have investigated the surface morphology of the synthesized $LiMnO_2$ nanoparticles using SEM method. The structural properties obtained using XRD and XPS. These results demonstrate that temperature plays a critical role in determining the phase purity and crystallinity of the sample. The purest orthorhombic structure of the $LiMnO_2$ nanoparticles was observed for the sample synthesized at 200°C for 14 h. $LiMnO_2$ based electrode ($LiMnO_2$:CB:PVA (80:11:9)) were coated onto an ITO/glass substrate using the Dr. Blade method. Then, the electrochemical properties of electrode were investigated using the three-electrode method. The highest amounts of intercalated and deintercalated charge densities were obtained for the purest orthorhombic $LiMnO_2$ phase. This simple and efficient synthesis method are a promising approach for future studies of o-$LiMnO_2$, as it has improved structural stability and electrochemical properties compared to other $LiMnO_2$ polymorphs, making it a potential candidate for use in high-performance lithium-ion batteries.

(Received June 4, 2025; accepted February 4, 2026)

Keywords: Cathode, Orthorhombic $LiMnO_2$, Hydrothermal synthesis, Electrochemical properties

1. Introduction

Lithium-ion batteries (LIBs) play an important role in a wide range of applications from portable electronic devices to electric vehicles, owing to their high energy density, long cycle life and low self-discharge rates. In lithium-ion batteries, the cathode material is one of the most critical components that determines key performance criteria such as energy density, cycle life, and safety. Because the cathode material directly affects the total capacity and operating voltage of a battery, the development of cathode materials is of great importance to make progress in the development of energy storage technologies [1]. The common cathode materials (Lithium cobalt oxide (LCO), Nickel Manganese Cobalt (NMC), and Lithium Iron Phosphate (LFP) have certain limitations and a new generation of cathode materials is required to achieve goals such as higher energy density, cost reduction and environmental sustainability with cost reduction [2]. Although $LiCoO_2$ is a widely used cathode material today, the search for alternative cathodes has increased owing to the fact that cobalt is an expensive element, human rights violations of workers and children working in mines, the toxic effect of waste on the environment, and the thermal instability it shows as it moves towards high temperatures. Therefore, many extensive studies have been conducted to develop effective cathode materials to increase the energy and power densities and improve the stability of LIBs, which are important factors for industrial production [3-6]. At this point, manganese-containing cathode materials, which are abundant and inexpensive have been proposed as an alternative to the materials commonly used today. In the quest to improve critical performance indicators such as energy density and cycle life of lithium-ion batteries, orthorhombic $LiMnO_2$ (o-$LiMnO_2$), which offers theoretically higher capacity and thermal stability potential compared to conventional cathode materials such as spinel-structured $LiMn_2O_4$ and layered $LiCoO_2$, stands out as a remarkable candidate for next-generation cathode materials [7]. $LiMnO_2$ is known to exist in several phases. Two phases, whose crystal structures have been well characterized, are a high temperature orthorhombic phase (Pmnm) and a tetragonal phase (I41/amd). Both structures involve cubic close packing but they differ in the arrangement of the ordering of the lithium and manganese cations [8]. It has a lot of metastable states including orthorhombic (o- $LiMnO_2$, space group Pmmn), monoclinic (m-$LiMnO_2$, space group C2/m), and layered $LiMnO_2$ (space group R3m) with α-$NaFeO_2$-like structure. Among these structures, the o-$LiMnO_2$ is the most stable one [9].

$LiMnO_2$ cathode materials are produced by many methods, including solid-state reactions, hydrothermal synthesis, sol-gel, and mechanochemical methods. Freire et al. synthesized a rock-salt type nanostructured $Li_4Mn_2O_5$ material, which showed the highest discharge

capacity reported for lithium manganese oxide electrode materials [10]. Liu et al. reported that $Li_4Mn_5O_{12}$ was synthesized by solid state reaction at low temperature and this cathode provided a high capacity of 212 mAh g^{-1} [11]. Many synthesis routes have been reported for the preparation of o-$LiMnO_2$; however, the synthesis methods vary greatly because of their impact on the resulting electrochemical performance, morphology, purity, and crystal structure. Zhao et al. prepared orthorombic $LiMnO_2$ nanorods via a simple and economical in-situ carbothermal reduction method using nanorod-like MnO_2 as manganese precursor [12]. Liu et al. prepared a pure phased o-$LiMnO_2$ powder employing Mn_2O_3 and LiOH as the raw material using a facile one-step hydrothermal routine [13]. It was found by the experiment that the hydrothermal temperature is the key factor that greatly influence the phase purity of the final o-$LiMnO_2$ product. The orthorhombic $LiMnO_2$/CNTs composite prepared via a one-step dynamic hydrothermal method with 5 wt% CNTs, exhibited optimal performance, delivering a specific capacity of 204.9 mAh g^{-1} and 97.7% capacity retention after 50 cycles due to effective conductive framework formation [14]. Wu et al. synthesized o-$LiMnO_2$ in liquid phase with a diameter of 35 nm by a 2-step hydrothermal method and obtained a high reversible capacity of 215 mAh g^{-1} [15]. Xliao et al. synthesized o-$LiMnO_2$ by a one-step hydrothermal method and reported that the nanoparticles exhibited a capacity 170 mAh g^{-1} witch consistent that reported in the literature [16].

In this study, o-$LiMnO_2$ particles were prepared based on the method previously prepared by Xiao et al. [16]. $LiOH{\cdot}H_2O$ was selected as lithium source and $MnSO_4{\cdot}H_2O$ was selected as manganese source. H_2O_2 was chosen as oxidizing agent. Although o-$LiMnO_2$ was obtained under suitable hydrothermal conditions, according to XRD analyses, o-$LiMnO_2$ could only be pure phase at a certain temperature and time.

2. Method and characterization

The $MnSO_4$ to LiOH molar ratio was maintained at 1:3. For this purpose, 3.4 g (20 mmol) $MnSO_4$ and 1.45 g (60 mmol) $LiOH{\cdot}H_2O$ were dissolved in 43 ml DI water. The mixture was vigorously stirred until it became homogenous. After the materials were completely mixed, 7 mL of 35% H_2O_2 was slowly added under stirring. As the reaction is exothermic, the temperature increases. Because of outgassing and foaming, H_2O_2 was slowly added using a micropipette. With the addition of H_2O_2, the initially pinkish-coloured mixture turned dark brown. The mixture was stirred vigorously with a magnetic stirrer until all the components were thoroughly dissolved. The stirred reactants were transferred to an autoclave (100 mL) and annealed at 180-200 °C for 12-14 hours and the system was allowed to cool down to room temperature. The final product was accumulated at the bottom of the Teflon liner. After filtration, the collected particles were washed several times with distilled water and ethanol, centrifuged, and air-dried overnight at 60 °C.

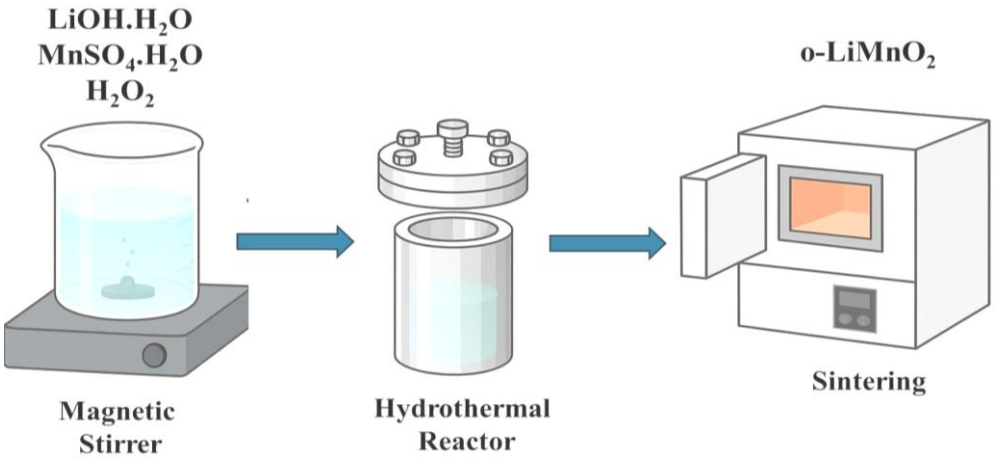

Fig. 1. The schematic illustration of synthesis of the sample (colour online)

When $MnSO_4{\cdot}H_2O$ is dissolved in water, the reaction equation is as follows.

$$MnSO_4 \cdot H_2O \rightarrow Mn^{2+} + SO_4^{2-} + H_2O$$

Hydrogen peroxide is;

$$H_2O_2 \rightarrow O_2 + 2H^+$$

The reaction is believed to carried out three stages. Firstly, LiOH and Mn^{2+} ions formed $Mn(OH)_2$ in solution, the Mn^{2+} ions was oxidized into Mn^{3+} ions by H_2O_2. Finally, Mn^{3+} containing precursor (e.g. $Mn(OH)_3$) react with the LiOH in the medium. Under high pressure and temperature the precursor form the final product $LiMnO_2$ [17].

$$MnSO_4 \cdot H_2O + LiOH{\cdot}H_2O + H_2O \rightarrow LiMnO_2$$

The surface morphology of the o-$LiMnO_2$ nanoparticles synthesized by the hydrothermal method was investigated using scanning electron microscopy (SEM).

The structural properties of the o-$LiMnO_2$ were determined by X-ray diffraction (XRD) and X-ray photoelectron spectroscopy (XPS). The electrochemical properties of the o-$LiMnO_2$ films were obtained using electrochemical analyzer with three-electrode method. For the electrochemical measurements, the o-$LiMnO_2$ films were deposited on an ITO glass substrate using a doctor blade. During the formation of the o-$LiMnO_2$ films, the active material (o-$LiMnO_2$), carbon black, and the binder material poly(vinyl alcohol) (PVA) were prepared at a weight ratio of 80:11:9. To this end, the active material ($LiMnO_2$) was ground in an agate mortar; then the carbon black was ground; and finally, the two were ground together in a mortar and mixed. In a separate beaker, 1 g of PVA and 20 ml of NMP (N-methylpyrrolidone) were heated and mixed at 60 °C for 48 hours, after which the desired amount of this mixture was added to the active material–carbon black mixture in the agate mortar. For the electrochemical measurement of the o-$LiMnO_2$ film, a 0.5 M $LiClO_4$-PC solution was used as the electrolyte, a Pt wire as the counter electrode, an Ag/AgCl electrode as the reference electrode, and an o-$LiMnO_2$-ITO-glass structure as the working electrode.

Qu et al. carried out electrochemical studies of ITO films at high potentials in an electrolyte of LiClO4 in propylene carbonate. They showed that ITO is stable enough to be studied at 6.0 V in a lithium-ion electrolyte, meaning that although it is kinetically limited compared to many other materials, it initially possesses high anodic stability [18].

3. Results and discussion

The phase structures of the obtained $LiMnO_2$ nanoparticles were identified using a Pananalytical (X'pert Pro MPD) XRD instrument. XRD patterns were collected over the angular range of 10–80º using Bragg–Brentano (BB) geometry (Cu K-α source, λ=1.5406 Å). Fig. 2 shows the XRD pattern of o-$LiMnO_2$ nanoparticles. Samples have narrow peaks, indicating that it is well crystallized. Each diffraction peak was accurately indexed in relation to the orthorhombic structure's space group (a = 2.805 Å, b = 5.757 Å, c = 4.527) Pmmn. The $LiMnO_2$ nanoparticles synthesized hydrothermally and subsequently annealed at 180-200°C for 12-14h, predominantly exhibited the orthorhombic phase of $LiMnO_2$. Additionally, a secondary and a tertiary phase were identified in the samples annealed for 12 hours, exhibiting a comparatively weak diffraction peak at approximately 2theta = 18° and 29°, respectively. These peaks were attributed to the presence of Mn_3O_4 (hausmannite) phases in sample.

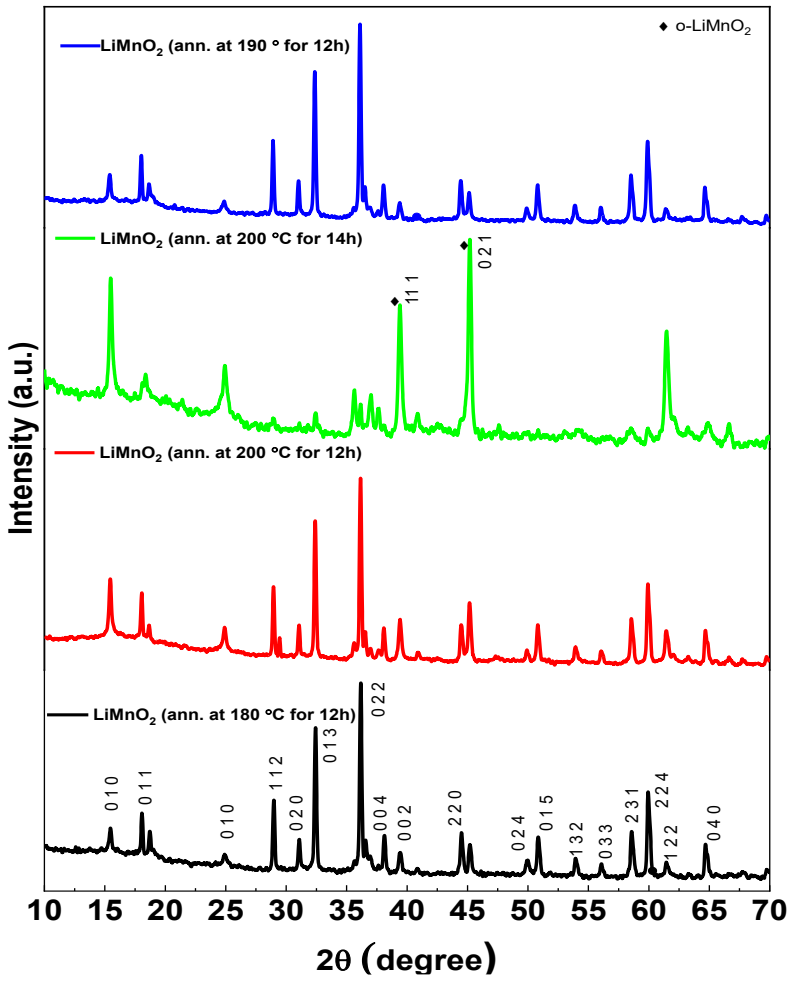

Fig. 2. XRD pattern of the $LiMnO_2$ nanoparticles synthesized at various conditions (colour online)

The surface morphologies of the $LiMnO_2$ particles annealed various temperatures and times in an atmospheric environment were investigated by scanning electron microscopy SEM (FESEM, FEI–Nova Nanosem 430), as were shown in Fig. 3a-d. Morphology can affect the energy barrier for Li^+ diffusion in several aspects, including grain boundaries, active area, and the distribution of crystal facets [19]. The average size of the $LiMnO_2$ particles synthesized using the hydrothermal method at 180, 190 and 200 °C for 12h and annealed at 200 °C for 14 h were obtained as 58, 74.61, 75.00, 76.56 nm, respectively. As a result of the increase in the temperature and annealing time, the size of the particles increased. It is believed that a subtle increase in particle size promotes enhanced crystallization and the formation of a more ordered surface morphology, consequently leading to a reduction in deleterious side reactions and thus contributing to more stable electrochemical measurements.

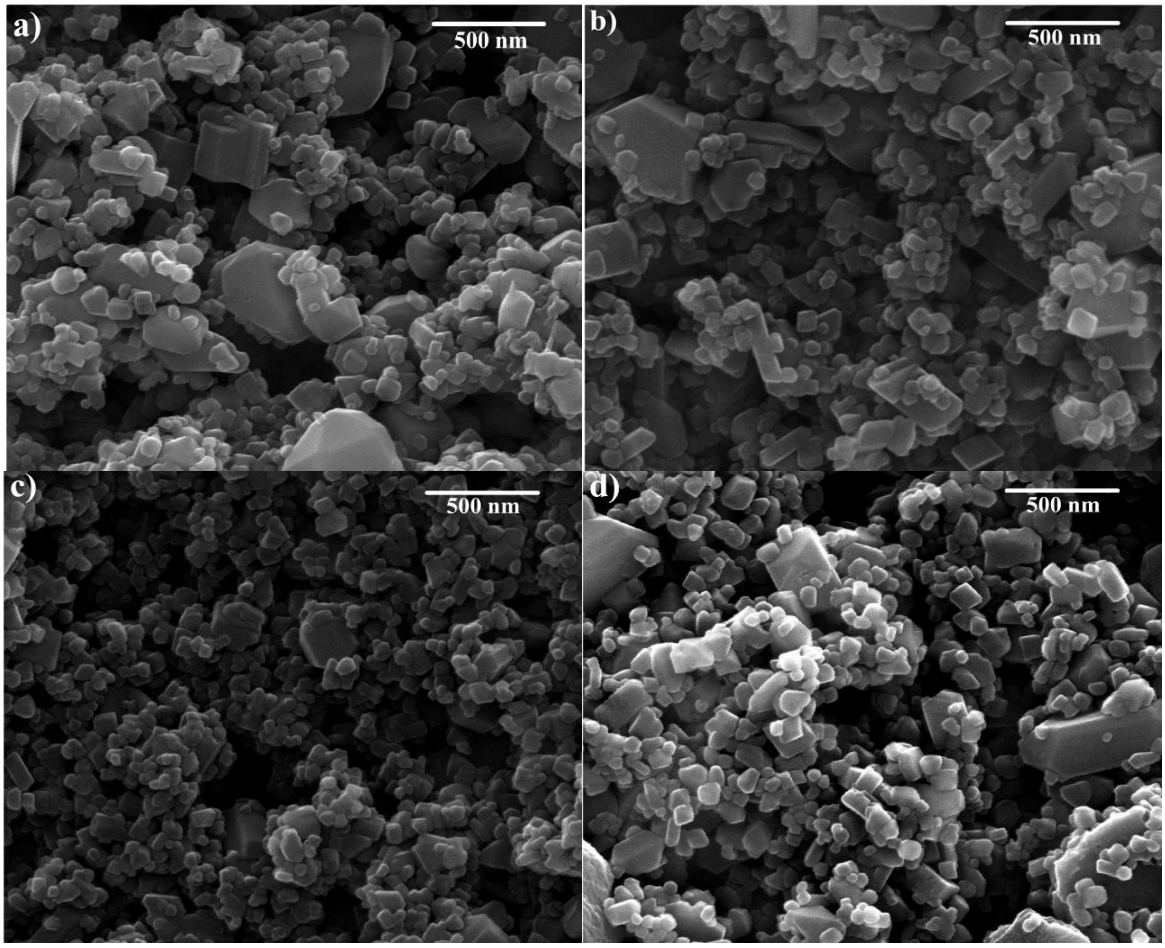

Fig. 3. SEM images of the surface morphology of hydrothermally synthesized o-$LiMnO_2$ nanoparticles at annealed a) 180 ºC for 12 h, b) 190 ºC for 12 h, c) 200 ºC for 12 h, and d) 200 ºC for 14 h (colour online)

The chemical composition and binding energies of the $LiMnO_2$ nanoparticles synthesized using the hydrothermal method were investigated by X-ray photoelectron spectroscopy. The Shirley model was used as a background model [20]. The reference carbon peak, positioned at a binding energy of 284.6 eV, was employed for the energy calibration of the samples [21]. Fig. 4 c-d shows the fitting of the O1s, Li1s and Mn2p peaks according to the C1s peak. The O1s peaks of the oxygen atoms in the $LiMnO_2$ nanoparticles were fitted using Gaussian convolution. According to the obtained O1s peaks, two Gaussian peaks contain (-OH) peaks due to the interaction between oxygen and the metal, as well as partial absorption due to environmental conditions (humidity etc.). These two peaks were located at 529.54 eV and 530.98 eV, respectively.

As can be seen in Figure 4c, in the high-resolution analysis of Mn, it was observed that the spectrum of the Mn atom at the core level consists of the peaks: Mn2p3/2 and Mn2p1/2. The Mn2p3/2 peak in the o-$LiMnO_2$ sample comprise of the coexistence of both Mn^{3+} and Mn^{4+} state. Calculations based on the ratio of peak areas show that the Mn^{3+} and Mn^{4+} ratios were approximately 49% and 51%, respectively. The binding energy of Mn2p3/2 of the

sample is in between binding energy of those in Mn_2O_3 (641.6 eV) and MnO_2 (642.6 eV) [22]. These peaks are located at 641.32 and 653.17 eV, respectively [23, 24]. As can be seen in Figure 4d, the Li1s peak was obtained at 54.56 eV. As previously reported, the Li1s peak values found here are consistent with those reported in the literature [9,24].

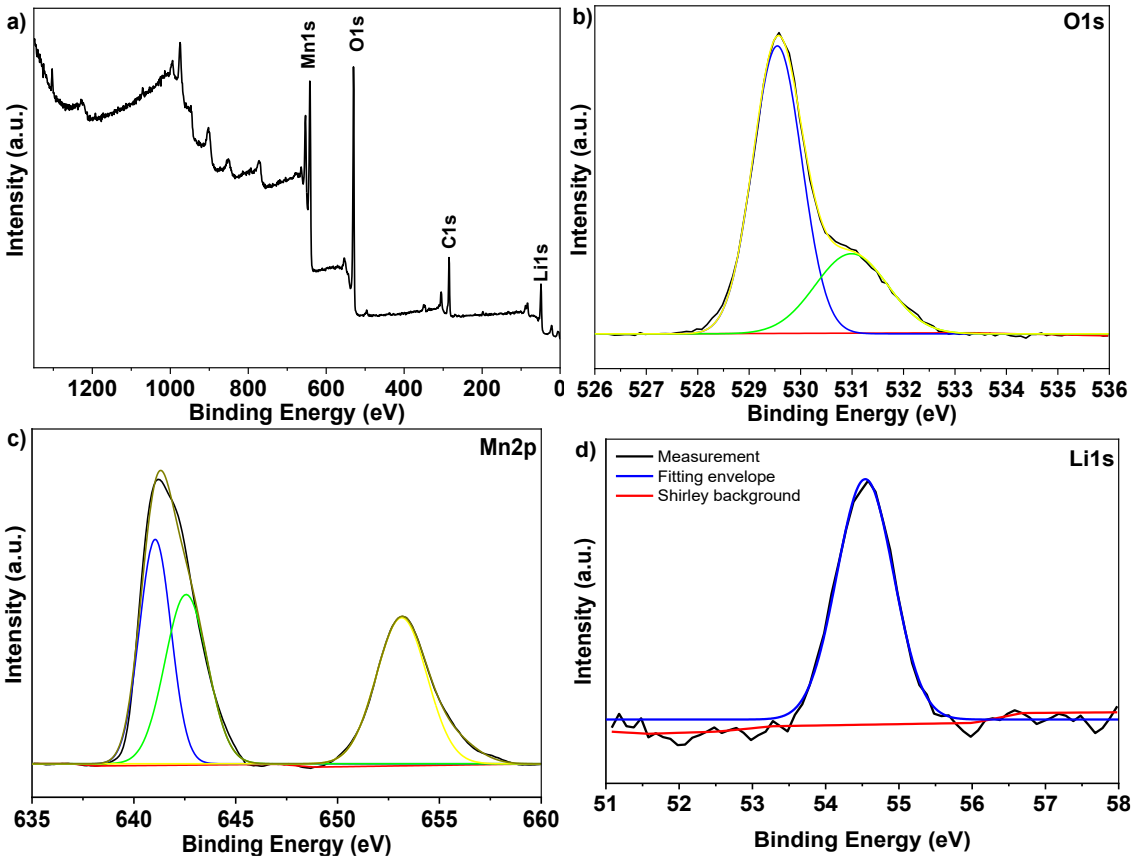

Fig. 4. XPS spectra of $LiMnO_2$ nanoparticles synthesized by hydrothermal method a) survey b) O1s, c) Mn2p ve d) Li1s XPS peaks (colour online)

4. Electrochemical measurements

The CV curves of o-$LiMnO_2$-ITO-glass electrodes with active material obtained by hydrothermal methods in 0.5 M $LiClO_4$/PC electrolyte solution at scan rates of 10, 20, 30, 40 and 50 mV/s in the range from –2 V to +2 V (Cyclic Voltammetry), as are given in Fig. 5a-d. It was observed that the area under the CV curves increased as the scan rate increased. Randles [25] and Sevcik [26] describe the effect of scan rate to current. According Randles–Ševčík eqn. diffusion current is proportional to $\sqrt{v}$ (v is the scan rate). Fig. 5e shows the CV curves at a scan rate of 20 mV/s. The CV curves of the electrodes prepared by using $LiMnO_2$ samples with a sintering temperature of 200 °C for 14 h were found to be wider. The specific capacitance C can be calculated from the CV curve using the following equations:

$$C = \frac{\int i(V)dV}{2km\Delta V}$$

$$\int_{V_1}^{V_2} i(V)dV = A\ (Area)$$

,

where i and V are the current and potential in the CV measurement, k is the scan rate (mV/s), m is the mass of active material (g), ΔV is the potential window of CV curve [27, 28]. C specific capacitance (in Fg^{-1}) was calculated by using m (in g) as the sum of the masses of the positive electrode (active material + $LiMnO_2$ + CB). Specific capacities of o-$LiMnO_2$ nanoparticles synthesized by hydrothermal method at varying temperature and sintering time were obtained as 180 °C for 12 h (165 mAh/g), 190 °C for 12 h (174 mAh/g), 200 °C for 12 h (176 mAh/g) and 200 °C for 14 h (224 mAh/g). Among the o-$LiMnO_2$ nanoparticles, the highest specific capacity of 224 mAh/g was obtained for the sample sintered at 200 °C for 14 h. Additionally, Fig. 5f demonstrates the CA curves measured under constant potential of ±2 V for 100 s at 50 s intervals. The amount of intercalated and deintercalated charge densities were calculated by using CA curves. The highest amount of intercalated and

deintercalated charge densities were calculated as 129.62 mC/cm^2 and 133.70 mC/cm^2 for $LiMnO_2$ electrode with a sintering temperature of 200 °C for 14 h, respectively.

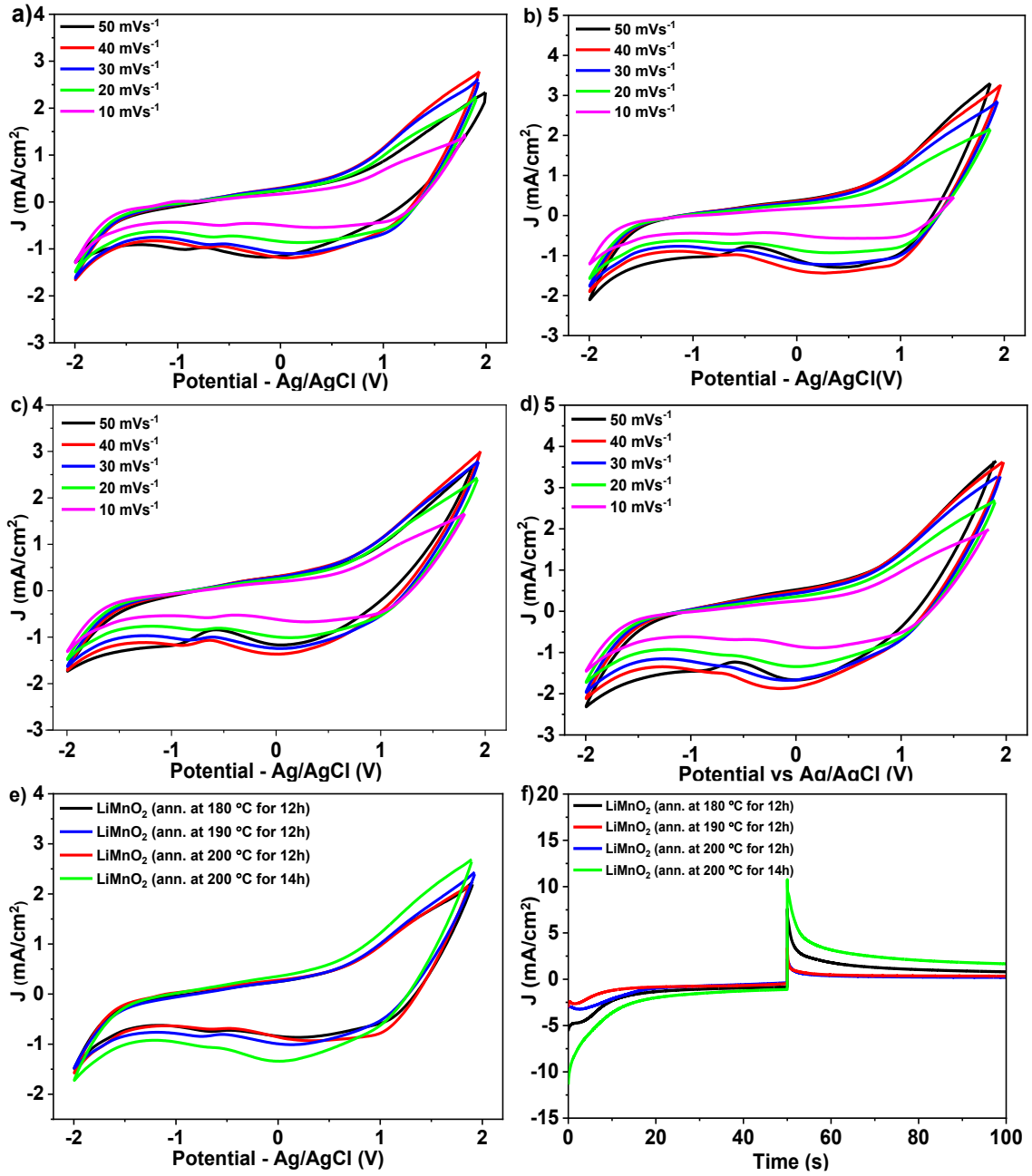

Fig. 5. CV curves of the samples synthesized at a) 180 ºC for 12 h, b) 190 ºC for 12 h, c) 200 ºC for 12 h, and d) 200 ºC for 14 h., e) CV curve at 20 mVs^{-1} scan rate of all samples f) CA curves for the corresponding sample (colour online)

The electrochemical impedance spectroscopy (EIS) measurements were performed at 0.05 V over a frequency range of 0.1 Hz–1.0 MHz to analyze the ion conducting properties of the synthesized samples. Fig. 6 shows the Nyquist plots of the o-$LiMnO_2$ electrode. The equivalent circuit of the structure is also inserted into Fig. 6. By demonstrating the electrochemical impedance of the material, it provides valuable information on lithium-ion intercalation/deintercalation kinetics and various resistance components on the electrode surface. EIS measurements, successfully fitted to the R(CR)(CR)W equivalent circuit, which represents the heterogeneous structure and interfacial properties of the system. Despite the visual appearance of a single depressed semicircle in the Nyquist plots, fitting analyses demonstrated that the highest accuracy (Error < 1.5%) was achieved with this two-time-constant model. In this circuit, R_s corresponds to the ohmic electrolyte resistance, while R_f and R_{ct} denote the contact resistance at the ITO/cathode interface and the charge transfer resistance, respectively. The linear tail observed in the low-frequency region is attributed to the Warburg impedance (W), associated with diffusion-

controlled processes [29]. Analysis results tabulated in Table 1, although all samples exhibited comparable ohmic resistance (R_s) values but optimization in annealing temperature is quantitatively supported by a monotonic decrease in resistive components. Crucially, the sample 4 achieved the lowest series resistance (R_s = 22.98 ohm) and exhibited a dramatic reduction in the high-frequency charge transfer resistance, R_{ct}, dropping from an initial 1241 ohm to 164.5 ohm. Sample 4 annealed at 200 °C for 14 h showed the lowest charge transfer resistance (R_{ct}), evidenced by the smallest semicircle diameter in the Nyquist plot, indicating that kinetic barriers at the electrode/electrolyte interface could be lowered. Decrease in the charge transfer resistance allows the electrode material to interact with lithium ions quickly and efficiently, while positively affecting the overall battery cell performance [30]. The decrease signifies profoundly improved bulk conductivity and accelerated charge-transfer kinetics. Simultaneously, both double layer capacitances (C_{dl1} and C_{dl2}) increased consistently, reaching their maximum (e.g., $C_{dl1} = 4.47 \times 10^{-8}$ F) for the sample 4, confirming an enhanced effective active surface area and charge storage capacity. Additionally, this sample also exhibited the lowest Warburg coefficient σ (0.002515) that confirms the inverse relationship between the Warburg coefficient and the diffusion coefficient $D_{Li} \propto \sigma^{-2}$ [31].

The diffusion coefficient (D) of Li^+ can be determined in the low-frequency region using Nyquist plots, as described by the following equation [32]:

$$D = R^2T^2/2A^2n^2F^4C^2\sigma^2$$

Herein T is absolute temperature, R is universal gas constant, n is the number of electrons, F is Faraday constant, C is the concentration of Li^+ ions (0.5 M $LiClO_4$/PC) and σ is Warburg coefficient.

The diffusion coefficient of lithium ions was calculated to be of the order of 10^{-8} (cm^2/s). The highest Li^+ diffusion coefficient of 9.56×10^{-8} cm^2/s was obtained for the sample synthesized at 200 °C for 14 h.

The ion conductivity of $LiMnO_2$ nanoparticles coated on ITO/glass was calculated by the following formula [33].

$$\delta = (1/R_b)(d/S)$$

where δ the ionic conductivity, R_b is the bulk resistance, d is the film thickness, S is the film area. The ionic conductivity of $LiMnO_2$ nanoparticles was calculated to be of the order of 10^{-6} S/cm and the highest ionic conductivity was obtained as 9.95×10^{-6} S/cm for the sample synthesized at 200 °C for 14 h. The result verifies that lithium-ion diffusion occurs most rapidly and efficiently within the crystal lattice of the sample. Therefore, the precise thermal treatment during the synthesis of the sample is an essential step for revealing the electrochemical storage capacity of the $LiMnO_2$.

Table 1. Fitting parameters of EIS Plots

Sample	Annealing Temperature	Rs (Ω)	Rf (Ω)	C_{dl1} (F)	Rct (Ω)	C_{dl2} (F)	Warburg Coefficient W
1	180 °C, 12h	33.82	280.2	2.70×10−9	1241.0	0.005192	0.076410
2	190 °C,12h	28.55	240.0	3.16×10−9	470.0	0.008486	0.014950
3	200 °C, 12h	26.92	215.0	1.47×10−8	210.0	0.011700	0.019260
4	200 °C, 14h	22.98	162.6	4.47×10−8	164.5	0.013050	0.002515

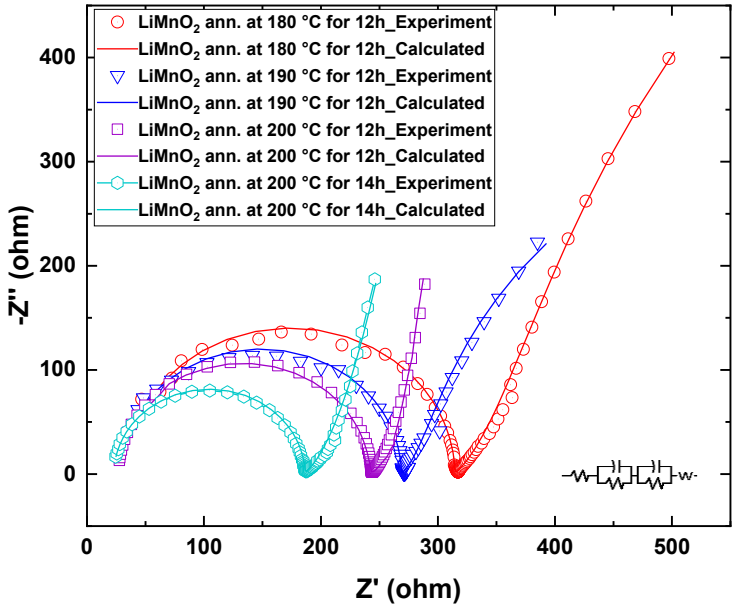

Fig. 6. Nyquist plot of $LiMnO_2$ nanoparticles (colour online)

5. Conclusion

The synthesis of o-$LiMnO_2$ particles via hydrothermal method followed by annealing at varying temperatures and durations yielded significant insights into optimal processing conditions. The properties of the samples synthesized between 180 °C and 200 °C for 12 to 14 h during hydrothermal process were investigated, with the most promising results observed in the specimen treated at 200 °C for 14 hours. This particular sample exhibited o-$LiMnO_2$ in its pure phase and demonstrated the largest particle size when examined under scanning electron microscopy. Electrochemical impedance spectroscopy measurements revealed that this sample also possessed the smallest resistance in the semicircle, indicating enhanced electrical conductivity. Furthermore, cyclic voltammogram of the sample possessing the largest area that is the indication of the highest amounts of intercalated and deintercalated charge densities during the electrochemical cycling. Chronoamperometry measurements also corroborated these findings, displaying the largest amount of intercalated-deintercalated charge capacity for the sample synthesized at 200 °C for 14h. These results show that synthesizing at 200 °C for 14h in one step hydrothermal process bring o-$LiMnO_2$ particles promising preliminary electrochemical behavior to be used in Li-based batteries.

References

[1] J. B. Goodenough, K.-S. Park, Journal of the American Chemical Society **135**(4), 1167 (2013).
[2] J. M. Tarascon, M. Armand, Nature **414**(6861), 359 (2001).
[3] S.-J. Bao, Y.-Y. Liang, W.-J. Zhou, B.-L. He, H.-L. Li, Journal of Colloid and Interface Science **291**(2), 433 (2005).
[4] S. Lee, Y. Cho, H.-K. Song, K. T. Lee, J. Cho, Angewandte Chemie-International Edition **51**(35), 8748 (2012).
[5] L. Xiao, Y. Zhao, Y. Yang, Y. Cao, X. Ai, H Yang, Electrochimica Acta **54**(2), 545 (2008).
[6] C. Zhang, X. Liu, Q. Su, J. Wu, T. Huang, A. Yu, ACS Sustainable Chemistry and Engineering **5**(1), 640 (2017).
[7] X. Li, D. Yu, V. S. Byg, S. D. Ioan, Journal of Energy Chemistry **82**, 103 (2023).
[8] I. J. Davidson, R. S. McMillan, J. J. Murray, J. E. Greedan, Journal of Power Sources **54**(2), 232 (1995).
[9] N. H. Vu, V.-D. Dao, H. H. T. Vu, N. V. Noi, D. T. Tran, M. N. Ha, T.-D. Pham, Journal of Nanomaterials **2021**(1), 9312358 (2021).
[10] M. Freire, N. V. Kosova, C. Jordy, D. Chateigner, O. I. Lebedev, A. Maignan, V. Pralong, Nature Materials **15**(2), 173 (2016).
[11] Y. Liu, G. Liu, H. Xu, Y. Zheng, Y. Huang, S Li, J. Li, Chemical Communications **55**(56), 8118 (2019).
[12] H. Zhao, J. Wang, G. Wang, S. Liu, M. Tan, X. Liu, S. Komarneni, Ceramics International **43**(13), 10585 (2017).
[13] Q. Liu, Y. Li, Z. Hu, D. Mao, C. Chang, F. Huang, Electrochimica Acta **53**(24), 7298 (2008).
[14] C. Shen, H. Xu, L. Liu, H. Hu, K.-F. Aguey-Zinsou, L. Wang, Journal of Alloys and Compounds **859**, 157834 (2021).
[15] M. Wu, Q. Zhang, H. Lu, A. Chen, Solid State Ionics **169**(1-4), 47 (2004).
[16] X. Xiao, L. Wang, D. Wang, X. He, Q. Peng, Y. Li, Nano Research **2**, 923 (2009).
[17] S. Zhao, K. Yan, J. Zhang, B. Sun, G. Wang, Angewandte Chemie International Edition **60**(5), 2208 (2021).
[18] H.-Y. Qu, E. A. Rojas-González, C. G. Granqvist, G. A. Niklasson, Thin Solid Films **682**, 163 (2019).
[19] Z. Meng, X. Ma, L. Azhari, J. Hou, Y. Wang, Communications Materials **4**(1), 90 (2023).
[20] A. Herrera-Gomez, M. Bravo-Sanchez, O. Ceballos-Sanchez, M. O. Vazquez-Lepe, Surface and Interface Analysis **46**(10-11), 897 (2014).
[21] M. C. Biesinger, Applied Surface Science **597**, 153681 (2022).
[22] C. D. Wagner, Handbook of x-ray photoelectron spectroscopy: a reference book of standard data for use in x-ray photoelectron spectroscopy, Perkin-Elmer Corp., USA, 1979.
[23] X. Li, Z. Su, Y. Wang, Journal of Alloys and Compounds **735**, 2182 (2018).
[24] Y.-K. Zhou, J. Huang, H.-L. Li, Applied Physics A **76**, 53 (2003).
[25] J. E. B. Randles, Transactions of the Faraday Society **44**(0), 327 (1948).
[26] A. Ševčík, Collection of Czechoslovak Chemical Communications **13**, 349 (1948).
[27] L. Huang, D. Chen, Y. Ding, Z. L. Wang, Z. Zeng, M. Liu, ACS Applied Materials and Interfaces **5**(21), 11159 (2013).
[28] D. Hulicova-Jurcakova, A. M. Puziy, O. I. Poddubnaya, F. Suárez-García, J. M. D. Tascón, G. Q. Lu, Journal of the American Chemical Society **131**(14), 5026 (2009).
[29] A. C. Lazanas, M. I. Prodromidis, ACS Measurement Science Au **3**(3), 162 (2023).
[30] X. Wang, X. Wei, H. Dai, Journal of Energy Storage **21**, 618 (2019).
[31] F. Gao, Z. Tang, Electrochimica Acta **53**(15), 5071 (2008).
[32] A. J. Bard, L. R. Faulkner, H. S. White, Electrochemical methods: fundamentals and applications, John Wiley and Sons, 2022.
[33] X. Qian, N. Gu, Z. Cheng, X. Yang, E. Wang, S. Dong, Journal of Solid State Electrochemistry **6**, 8 (2001).

*Corresponding authors: cihadkucukarslan@hacettepe.edu.tr
duyar@hacettepe.edu.tr